

Electron-ion recombination of Si IV forming Si III: Storage-ring measurement and multiconfiguration Dirac-Fock calculations

E. W. Schmidt, D. Bernhardt, A. Müller, and S. Schippers
*Institut für Atom- und Molekülphysik, Justus-Liebig-Universität,
 Leihgesterner Weg 217, 35392 Giessen, Germany*

S. Fritzsche
*Institut für Physik, Universität Kassel, Heinrich-Plett Strasse 40, 34132 Kassel, Germany**

J. Hoffmann, A. S. Jaroshevich,[†] C. Krantz, M. Lestinsky,[‡] D. A. Orlov, and A. Wolf
Max-Planck-Institut für Kernphysik, Saupfercheckweg 1, 69117 Heidelberg, Germany

D. Lukić[§] and D. W. Savin
*Columbia Astrophysics Laboratory, Columbia University,
 550 W. 120th St., MC 5247 New York, NY 10027, USA*
 (Dated: July 12, 2021)

The electron-ion recombination rate coefficient for Si IV forming Si III was measured at the heavy-ion storage-ring TSR. The experimental electron-ion collision energy range of 0–186 eV encompassed the $2p^6 nl n'l'$ dielectronic recombination (DR) resonances associated with $3s \rightarrow nl$ core excitations, $2s 2p^6 3s nl n'l'$ resonances associated with $2s \rightarrow nl$ ($n = 3, 4$) core excitations, and $2p^5 3s nl n'l'$ resonances associated with $2p \rightarrow nl$ ($n = 3, \dots, \infty$) core excitations. The experimental DR results are compared with theoretical calculations using the multiconfiguration Dirac-Fock (MCDF) method for DR via the $3s \rightarrow 3p n'l'$ and $3s \rightarrow 3d n'l'$ (both $n' = 3, \dots, 6$) and $2p^5 3s 3l n'l'$ ($n' = 3, 4$) capture channels. Finally, the experimental and theoretical plasma DR rate coefficients for Si IV forming Si III are derived and compared with previously available results.

PACS numbers: 34.80.Lx, 36.20.Kd, 95.30.Dr, 98.58.Bz.

Keywords: atomic data — atomic processes

I. INTRODUCTION

Spectroscopic [1] observations of absorption lines in the intergalactic medium (IGM) can be used to study the origin of large-scale structure in the universe, the history of star and galaxy formation, the metagalactic radiation field, and the chemical evolution of the IGM [2, 3, 4]. Observations of lines from C IV, N V, O VI, and Si IV are routinely employed for these studies. These observations provide important constraints for IGM studies when coupled with calculations of the ionization balance using codes such as CLOUDY [5]. However, the accuracy with which one can infer the properties of the IGM is limited by uncertainties in the underlying atomic data.

Of particular importance are reliable electron-ion recombination data for the process known as dielectronic recombination (DR). This is the dominant recombination process for most atomic ions under IGM conditions. Recently, Savin [2] has investigated the importance of

DR for C IV, N V, O VI, and Si IV. (Here, the convention of identifying each ion by its charge state before the recombination process is used.) His work has shown that uncertainties in the DR data for these four ions limit our ability to constrain the metagalactic radiation field and the initial mass function for the earliest generations of stars.

In the last several years, a series of measurements has been carried out to produce accurate DR data for C IV [6], N V [7], O VI [8], and sodium-like Si IV which will be presented in this work. Other experimental results for DR rate coefficients of Na-like ions have been published for Si IV [9], for Fe XVI [10] and for Ni XVIII [11]. Recently detailed calculations of the low energy DR resonance structure have been performed for Si IV [12] within the framework of relativistic many-body perturbation theory (RMBPT).

In the present work, experimental results for the Si IV recombination rate coefficient are presented. These were obtained employing the electron-ion merged-beams method at a heavy-ion storage ring. Orban et al. [9] measured the Si IV recombination rate coefficient in the electron-ion collision energy range 0–20 eV that comprises DR resonances associated with $3s \rightarrow 3p$ and $3s \rightarrow 3d$ ($\Delta N = 0$) core excitations. Here an extended energy range of up to 186 eV was experimentally investigated. This additional range includes DR resonances associated with $3s \rightarrow nl$ ($n \geq 4$), $2p \rightarrow nl$ ($n = 3, \dots, \infty$)

*Present address: Gesellschaft für Schwerionenforschung (GSI), Planckstrasse 1, D-64291 Darmstadt, Germany

[†]Permanent address, Institute of Semiconductor Physics, 630090 Novosibirsk, Russia

[‡]Present address: Columbia Astrophysics Laboratory, Columbia University, 550 W. 120th St., MC 5247 New York, NY 10027, USA

[§]On leave from the Institute of Physics, 10001 Belgrade, Serbia

($\Delta N = 1, 2, \dots$) and $2s \rightarrow nl$ ($n = 3, 4$) ($\Delta N = 1, 2$) core excitations. The corresponding excitation energies are listed in Table I, except those for $2s \rightarrow nl$ excitation. The present experimental Si IV merged-beams recombination rate coefficient thus benchmarks theory for light, low charged sodium-like ions over a wide range of energies.

TABLE I: Excitation energies E_{exc} for the excitation of Si IV $2s^2 2p^6 3s^2 S_{1/2}$ ground state to $2p^6 nl$ and to $2p^5 3s nl$ (both $n = 3, 4$) states that are relevant in the present work. For the derivation of the $2p^5 3s nl$ energies, results from experimental Auger spectroscopy [13] were added to the Si IV ionization energy of 45.14179 eV [14].

excited state	E_{exc} (eV)	Reference
$2p^6 3p^2 P_{1/2}$	8.839	[15]
$2p^6 3p^2 P_{3/2}$	8.896	[15]
$2p^6 3d^2 D_{5/2}$	19.884	[14]
$2p^6 3d^2 D_{3/2}$	19.884	[14]
$2p^6 4s^2 S_{1/2}$	24.050	[14]
$2p^6 4p^2 P_{1/2}$	27.062	[14]
$2p^6 4p^2 P_{3/2}$	27.082	[14]
$2p^6 4d^2 D_{5/2}$	30.997	[14]
$2p^6 4d^2 D_{3/2}$	30.997	[14]
$2p^6 4f^2 F_{5/2}$	31.508	[14]
$2p^6 4f^2 F_{7/2}$	31.508	[14]
$2p^5 3s^2 P_{3/2}$	99.06	[13]
$2p^5 3s^2 P_{1/2}$	99.68	[13]
$2p^5 3s 3p (^3P) ^4S_{3/2}$	104.8	[13]
$2p^5 3s 3p (^3P) ^4D$	106.2	[13]
$2p^5 3s 3p (^3P) ^4P$	106.9	[13]
$2p^5 3s 3p (^3P) ^2D$	107.5	[13]
$2p^5 3s 3p (^3P) ^2S_{1/2}$	108.4	[13]
$2p^5 3s 3p (^1P) ^2D_{5/2}$	110.9	[13]
$2p^5 3s 3p (^1P) ^2D_{3/2}$	111.5	[13]
$2p^5 3s 3p (^1P) ^2P$	112.0	[13]
$2p^5 3s 3p (^1P) ^2S_{1/2}$	112.7	[13]
$2p^5 3s 3d (^3D) ^4P_{3/2}$	119.2	[13]
$2p^5 3s 3d (^3D) ^4F$	119.9	[13]
$2p^5 3s 3d (^3D) ^4D_{7/2}$	121.1	[13]
$2p^5 3s 3d (^1D) ^2F_{7/2}$	124.1	[13]
$2p^5 3s 3d (^1D) ^2D_{3/2}$	124.6	[13]
$2p^5 3s 3d (^1D) ^2D_{1/2}$	125.1	[13]
$2p^5 3s (^3P) 4s ^4P_{3/2}$	125.8	[13]
$2p^5 3s (^3P) 4s ^2P$	126.3	[13]
$2p^5 3s (^1P) 4s ^2P_{3/2}$	126.9	[13]
$2p^5 3s 4p (^3P) ^4S$	128.4	[13]
$2p^5 3s 4p (^3P) ^2P$	129.5	[13]
$2p^5 3s 4p (^1P) ^2P$	131.0	[13]
$2p^5 3s 4d (^3D) ^4F$	133.3	[13]
$2p^5 3s 4d (^3D) ^2P$	134.7	[13]

In this work, the experimental results are compared to theoretical results using the multiconfiguration Dirac-Fock (MCDF) method, in particular at low electron-ion collision energies. At these energies, the calculation of accurate resonance positions and strengths is extremely critical for the derivation of reliable plasma DR rate coefficients. Therefore, the present work is partly an investi-

gation into the capabilities of the MCDF method for calculating accurate DR resonance energies and strengths. The MCDF method is an ab-initio method that is applicable to target atoms and ions with an arbitrary shell structure. In contrast, the RMBPT is currently limited to quasi one-electron target ions, owing to its inherent complexity. For such systems, however, it usually yields more accurate results than any other theoretical method. Below, a detailed comparison between the present MCDF results and the RMPBT results of Orban et al. [12] for DR of sodiumlike Si IV will be presented.

The present paper is organized as follows. The theoretical procedure is outlined in Section II. In Section III the experimental procedure is described. Experimental and theoretical results are presented and compared in Section IV. The Si IV to Si III experimental and theoretical DR rate coefficients in a Maxwellian plasma are derived and compared to recent theoretical and experimental results in Section V. Conclusions will be presented in Section VI.

II. THEORY AND IMPLEMENTATION

In most computations, DR of an \mathcal{N} -electron target ion in the initial state $|i\rangle$ is handled as a two-step process in which first an electron is captured resonantly from the continuum forming an $(\mathcal{N} + 1)$ -electron state $|d\rangle$ with the captured electron and one of the target core electrons both now in an excited level. In a second step, this doubly excited state either decays radiatively by the emission of one or more photons to some final state $|f\rangle$ which lies below the ionization threshold of the ion, or it returns by Auger electron emission to the initial ionization stage of the target. If interference between the radiative and nonradiative capture of the electron in the field of the target is negligible, the integrated DR cross section for an isolated resonance, the so-called resonance strength, can be expressed in terms of the Auger and radiative rates of the intermediate state $|d\rangle$ by

$$S(i \rightarrow d \rightarrow f) \equiv \int_{-\infty}^{\infty} \sigma_{\text{DR}}(E) dE \\ = \frac{2\pi^2 \hbar}{k_i^2} \frac{A_a(i \rightarrow d) A_r(d \rightarrow f)}{\Gamma_d}, \quad (1)$$

where k_i denotes the wave number and E the energy of the incident electron, Γ_d the width of the doubly-excited state, and $A_a(i \rightarrow d)$ is the rate for the dielectronic capture from the initial into the doubly excited state. Using the principle of detailed balance, the dielectronic capture rate $A_a(i \rightarrow d)$ is equal to $[g_d/g_i A_a(d \rightarrow i)]$ where $A_a(d \rightarrow i)$ is the Auger rate, and g_i and g_d are the statistical factors of the initial and intermediate states, respectively. $A_r(d \rightarrow f)$ refers to the rate for the radiative stabilization to the state $|f\rangle$. The strength as defined by Equation (1) refers to the area under the DR cross section curve. Hence, it is usually given in units of $\text{cm}^2 \text{eV}$. The

total width Γ_d is determined by all possible decay channels of the resonant state $|d\rangle$ and is given, in first-order perturbation theory, by

$$\Gamma_d = \hbar \left(\sum_j A_a(d \rightarrow j) + \sum_{f'} A_r(d \rightarrow f') \right), \quad (2)$$

where the sums are over all the individual Auger and radiative rates (widths) of the intermediate state $|d\rangle$. The use of the resonance strength $S(i \rightarrow d \rightarrow f)$ is appropriate for resonances whose width Γ_d is small compared to its energy position $E_{\text{res}} = E_d - E_i$ where E_d and E_i are the energy of the doubly excited state and initial state of the target ion, respectively, and if the energy dependent DR cross section has a Lorentzian profile [16]

$$\sigma_{\text{DR}}(E) = \frac{S}{\pi} \frac{\Gamma_d/2}{(E_{\text{res}} - E)^2 + \Gamma_d^2/4}. \quad (3)$$

Owing to the energy of the incident electron [cf. the $1/k_i^2$ factor in S], the resonance strength increases rapidly towards the DR threshold and makes the process sensitive to low kinetic energies of the incoming electrons.

At storage rings, the radiative stabilization is often not observed explicitly and, hence in Equation (1), the radiative rate for the individual transition $d \rightarrow f$ has to be replaced with

$$A_r(d \rightarrow f) \longrightarrow \sum_{f''} A_r(d \rightarrow f''),$$

where the summation extends over all states $|f''\rangle$ below the ionization threshold that can be reached by radiative transition from the doubly excited state $|d\rangle$. As seen from Equation (1), the observed DR strength for a given resonance is proportional to the capture rate $A_a(i \rightarrow d)$ and the total radiative rate. For most light and medium elements, moreover, the magnitude of the resonance strengths is often determined by the radiative decay since the emission of photons from the doubly excited state is then much slower than its autoionization and, hence, $A_a A_r / (A_a + A_r) \approx A_r$.

The doubly excited state $|d\rangle$ is often one out of a large number of highly correlated states embedded in the continuum of the target ion. For these resonances, special care has to be taken in calculating both the individual as well as total rates accurately. To describe the ground and excited state of multiply charged ions, the MCDF method has been found to be a versatile tool for the computation of the many-electron energies and decay properties, especially if inner-shell electrons or several open shells are involved in the computations [17, 18]. In the MCDF method, an atomic state is approximated by a linear combination of so-called configuration state functions (CSF) of the same symmetry

$$\psi_\alpha(PJ) = \sum_{r=1}^{n_c} c_r(\alpha) |\gamma_r PJ\rangle, \quad (4)$$

where n_c is the number of CSF, $\{c_r(\alpha)\}$ denotes the representation of the atomic state in this CSF basis, P is the parity, J is the total angular momentum, and γ_r is a set of quantum numbers for a unique specifying of the many-electron basis states. In most standard computations, the CSF are constructed as antisymmetrized products of a common set of orthonormal orbitals and are optimized on the basis of the Dirac-Coulomb Hamiltonian. Further relativistic contributions to the representation $\{c_r(\alpha)\}$ of the atomic states are then added, owing to the given requirements, by diagonalizing the Dirac-Coulomb-Breit Hamiltonian matrix in first-order perturbation theory. For multiply charged ions, an estimate of the dominant QED contributions (i.e., the self-energy and vacuum polarization of the electronic cloud) might be taken into account by means of scaled hydrogenic values. But QED plays a negligible role for Si^{3+} ions in the present analysis.

Obviously, the calculation of the radiative and nonradiative decay rates of the intermediate resonances $|d\rangle$ is central to the computation of any DR spectrum which is to be compared with experiment. In the MCDF model, both the radiative as well as the Auger matrix elements are derived from computation of the corresponding interaction matrix within the CSF basis using the expansion (4). To determine the rates, the wave functions from the GRASP92 [19] and RATIP [20] codes have been applied in the present work which allows one to incorporate both the dominant relativistic and correlation effects on the same footings. However, since the computation of the transition probabilities has been considered at many places elsewhere [18, 19], we shall mention here only that the radiative rates

$$A_r(d \rightarrow f) = \frac{4}{3c^2} \frac{\omega_{d \rightarrow f}^3}{2J_d + 1} \times \sum_{L\pi} |\langle \psi_f(J_f P_f) | H_\gamma(\pi L) | \psi_d(J_d P_d) \rangle|^2, \quad (5)$$

where $\omega_{d \rightarrow f}$ is the emitted photon's frequency, are associated with the reduced matrix elements of the interaction $H_\gamma(\pi L)$ of the atomic electrons with the multipole components of the radiation field [21], where $\pi = 0$ and $\pi = 1$ refer to electric and magnetic multipoles, respectively, with the multipolarity L . For light and medium elements, it is of course sufficient to include the electric-dipole ($L = 1$, $\pi = 1$) decay while the contributions from higher multipoles to the radiative stabilization remain negligible. To obtain the total radiative rate, i.e., to include the summation over all lower states $|f'\rangle$ in Equation (2), often a large number of transition rates have to be compiled with similar accuracy. For this reason the computation of the DR spectrum at higher energies may become difficult. In the RATIP program, the transition probabilities are computed by the REOS component [22] including, if appropriate, the rearrangement of the electron density in course of the decay. The explicit consideration of the electron density's rearrangement was not included here, because this would require separate calcu-

lations for the intermediate resonance states and the final states of the radiative stabilization. In the present calculations, however, both sets of states were always treated together in order to keep the computations feasible.

Unlike the treatment of radiative stabilization, calculation of the Auger rates requires the coupling of the bound-state electrons (of the target ion) to the electron continuum. If, for the sake of simplicity, we neglect the interaction between different Auger channels (i.e. *within the continuum*), the Auger rates are given by

$$A_a(d \rightarrow j) = 2\pi \times \sum_{\kappa_c} | \langle (\psi_j(J_j P_j), \epsilon \kappa_c) J_d P_d | H - E_d | \psi_d(J_d P_d) \rangle |^2, \quad (6)$$

where H is the atomic Hamiltonian, E_d the total energy of the doubly excited state and $\epsilon = E_d - E_j$ the kinetic energy of the emitted electron. In Equation (6), the summation over $\kappa_c = \pm(j_c + 1/2)$ for $l = j_c \pm 1/2$, where l and j_c are the angular momentum and total angular momentum, respectively, of the incoming or outgoing electron, extends over all partial waves of the outgoing electron which can be coupled to the target ion state $|\psi_j(J_j, P_j)\rangle$ with the condition to conserve the total angular momentum J_d and parity P_d of the intermediate state. If, moreover, a common set of *orthonormal* orbitals is used for the representation of the intermediate state $|d\rangle$ and the final ionic states $|j\rangle$, then the operator $(H - E) \approx V$ can be replaced by the electron-electron interaction operator. For most light and medium elements, it is again sufficient to include the instantaneous Coulomb repulsion between the electrons but to omit the relativistic Breit contributions as they were found important only for the Auger emission of highly-charged ions [23, 24, 25, 26].

The restriction of the electron-electron interaction in the computation of the matrix elements in Equation (6) is common practice, even though the orbital functions for the doubly excited state $|d\rangle$ and the final ionic state $|j\rangle$ are not quite orthogonal to each other. This treatment has been implemented therefore also in the AUGER component of the RATIP program, in which the continuum spinors are solved within a spherical but level-dependent potential of the final ion (the so-called *optimal level* scheme in the GRASP92 program). This scheme also includes the exchange interaction of the emitted electron with the bound-state density. Often, the number of the possible scattering states $|(\psi_j(J_j P_j), \epsilon \kappa_c) J_d P_d\rangle$ of a system increases rapidly with the number of intermediate ion states as the free electrons may couple in quite different ways to the bound-state electrons. For further details on the computations of the Auger matrix elements and relative intensities, we refer the reader to [18] and [27].

Apart from the individual rates, any helpful calculation of DR spectra critically depends on the proper control and handling of the various decay branches which, at least in principle, should be treated on the same basis in order to obtain a consistent spectrum. This need for an efficient handling of the decay channels concerns those

open-shell configurations in which one-particle excitations with large principal quantum numbers ‘mix into’ the low-energy part of the DR spectrum. Such a mixing occurs especially for the excitation of electrons beneath the valence shell whose energies are comparable with the valence excitation into Rydberg states. Therefore, in order to facilitate this handling of the various decay branches, a new component (DIEREC) has been developed recently in the framework of the RATIP program. This component now supports both, the computation of individual $S(i \rightarrow d \rightarrow f)$ and total resonance strengths $S(i \rightarrow d)$ and enables us to *simulate* the low-energy DR spectra as observed by experiment. Internally, of course, this new component makes use of the REOS and AUGER components from above and allows us, if necessary, to incorporate also higher multipoles in the computation of the (total) radiative rates. Because of the finite-difference method of the GRASP92 and RATIP programs and owing to the associated size of the configuration expansions, however, excitation to states with principal quantum numbers $n \gtrsim 8$ can often not be treated by the code explicitly. Atomic structure codes, such as, e.g., AUTOSTRUCTURE [28], that are geared towards the generation of DR rate coefficients for plasma physical applications, treat high- n electrons within a hydrogenic approximation. This has not yet been implemented in the RATIP program suite.

III. EXPERIMENT

The experiment was performed at the heavy-ion storage ring TSR of the Max-Planck-Institut für Kernphysik (MPI-K) in Heidelberg, Germany. Details of the merged-beams technique using the MPI-K electron cooler have been described previously [6, 29, 30, 31, 32].

In the present experiment a beam of $^{28}\text{Si}^{3+}$ was provided by the tandem accelerator of the MPI-K linear accelerator facility at an energy of about 1.1 MeV/u. The ion beam was injected into the storage ring where it was collinearly overlapped with the cooler electron beam. For efficient electron cooling, the electron velocity has to be close to the ion velocity in the ring. To fulfill this velocity-matching condition, the laboratory energy of the electrons was set to the ‘cooling’ energy $E_c \approx 593$ eV. The beam current was accumulated by multi-turn injection and ‘ecool stacking’ [33]. Ion currents of typically 10–50 μA were reached.

In contrast to previous experiments, where the electron beam of the cooler was also used as an electron target for recombination experiments, in the present experiment a newly installed separate electron beam [34] was used. This additional electron beam is hereafter denoted as the electron target. As in the electron cooler, the electron beam of the electron target is also guided by a magnetic field and overlaps the ion beam in a straight section of ≈ 1.5 m length.

Conceptually, the experimental procedures for measur-

ing recombination rate coefficients with the electron target are the same as those applied previously with the electron cooler. However, there are advantages when a separate electron target is employed for recombination measurements. First, the electron cooler can be used continuously for the cooling of the ion beam. Thus, the low velocity and spatial spread of the ion beam is maintained at all times. Second, the electron target was specifically designed for providing an electron beam with a very low initial energy spread [34]. Both advantages yield a higher experimental resolution in the present measurement as compared to previous measurements using only the electron cooler.

After injection into the storage ring, the ions were cooled for a few seconds before the recombination measurements started. Recombined ions were separated from the circulating beam in the first dipole magnet downstream of the electron target and counted by a single particle scintillation detector with nearly 100% efficiency. During the recombination measurement, the electron energy of the electron target beam was alternately chopped between measurement (E_m) and reference (E_r) energies by switching the acceleration voltage for the target electron beam accordingly. At the same time the electron cooler was held constant at cooling energy. The reference measurement was made to determine detector background. Therefore, the reference energy E_r was chosen in a range of the spectrum where no DR resonances occurred. The measurement and reference interval of data collection were 10 ms each. Between the voltage jump and the data collection interval there was a settling time of 5 ms to allow the power supplies to reach the preset values. The data were collected in overlapping data sets ranging from laboratory energies $E_m = 561$ eV to $E_m = 1420$ eV. The chopping pattern was $E_m^\nu - E_r - E_m^{\nu+1} - E_r$ with $\nu = 1, 2, 3, \dots$. With each step ν in the chopping pattern E_m was changed by 0.15 eV in the laboratory frame whereas E_r was kept fixed. The merged-beams rate coefficient is derived from the background subtracted recombination count rate using [29, 35]

$$\alpha(E_m) = \frac{[R(E_m) - R(E_m, E_r)]}{(1 - \beta_i \beta_e) \eta n_e(E_m) N_i L / C} + \alpha(E_r) \frac{n_e(E_r)}{n_e(E_m)}, \quad (7)$$

where R is the recombination count rate, η is the detection efficiency, n_e is the electron density in the interaction region, N_i is the number of ions in the ring and $C = 55.4$ m is the circumference of the TSR. In a first approach the nominal length L of the electron-ion overlap region in the electron target section is set to $L = 1.476$ m which is the length of the solenoid providing the axial magnetic field along the interaction region. For the detailed analysis we applied a toroid correction [30] that accounts for the contribution of the merging and de-merging sections in the toroidal magnetic fields of the electron target. The ion velocity and the electron velocity are $v_i = \beta_i c$ and $v_e = \beta_e c$, respectively, where c is the speed of light. Under the present conditions, the factor $1/(1 - \beta_i \beta_e)$ deviates by less than 0.4% from unity. The

second term in Equation (7) is a small correction that re-adds the recombination rate coefficient $\alpha(E_r)$ at the reference point. This contribution was calculated using a hydrogenic formula [6] for nonresonant radiative recombination (RR). The systematic experimental uncertainty of the merged-beams rate coefficient is estimated to be $\pm 18\%$ at 1σ confidence level. This uncertainty stems mostly from the ion current measurement ($\pm 15\%$ including also the error of the toroid correction) [30] and the determination of the electron density ($\pm 10\%$).

The experimental electron energy distribution is best described as a flattened Maxwellian distribution which is characterized by the longitudinal and transverse temperatures T_{\parallel} and T_{\perp} . The experimental energy resolution is approximately given by $\Delta E = [(\ln(2) k_B T_{\perp})^2 + 16 \ln(2) E k_B T_{\parallel}]^{1/2}$, where E denotes the relative electron-ion energy. For the reduction of T_{\perp} the target electron beam was adiabatically expanded [31] by factors of up to 28.

For the measurements we used two different cathodes, a thermionic cathode and a photocathode [36]. The electron current produced by the thermionic cathode was 4 mA and that of the photocathode 0.5 mA.

The cryogenic photocathode provides electrons with a laboratory energy spread of about 10 meV [36]. The expansion factor was 20. The electron beam temperatures were estimated by fitting a simulated (Sec. IV A) merged-beams recombination rate-coefficient comprising contributions by DR and RR to the measured spectrum. A transverse temperature of $k_B T_{\perp} \approx 0.9$ meV and a longitudinal temperature of $k_B T_{\parallel} \approx 35$ μ eV were found. With the above given temperature values, the experimental energy spread in the center of mass frame thus amounts to $\Delta E = 6$ meV at $E = 0.1$ eV, $\Delta E = 20$ meV at $E = 1$ eV, $\Delta E = 62$ meV at $E = 10$ eV, and $\Delta E = 197$ meV at $E = 100$ eV.

The temperature of the thermionic cathode is typically about 1300 K. The expansion factor was 28. The temperatures were again derived by fitting a simulated spectrum to the measured one. A transverse temperature of $k_B T_{\perp} \approx 4.4$ meV and a longitudinal temperature of $k_B T_{\parallel} \approx 100$ μ eV were determined. With these temperatures, the experimental energy spread thus amounts to $\Delta E = 11$ meV at $E = 0.1$ eV, $\Delta E = 33$ meV at $E = 1$ eV, $\Delta E = 105$ meV at $E = 10$ eV, and $\Delta E = 333$ meV at $E = 100$ eV.

IV. MERGED-BEAMS RATE COEFFICIENTS

A. Experimental results

Figure 1 shows the measured merged-beams recombination rate coefficient in the energy range 0–9.2 eV. For this measurement the photocathode was used. In this range all DR resonances associated with $3s \rightarrow 3p$ core excitations appear. The Rydberg series of $2p^6 3pn'l'$ DR resonances converges to its series limit at $E_{\infty} = 8.877$ eV

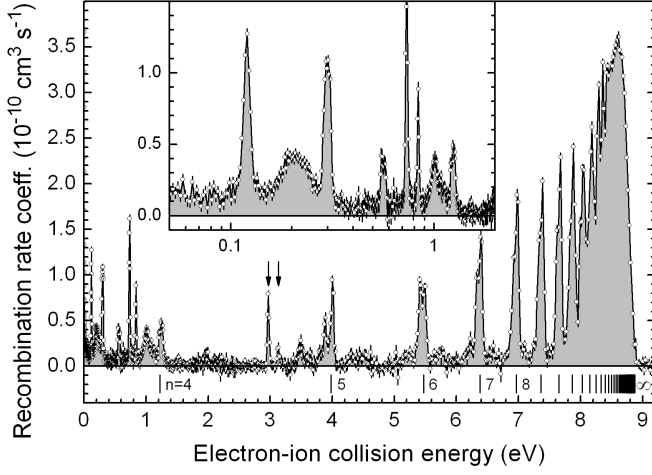


FIG. 1: Measured Si IV to Si III merged-beams electron-ion recombination rate coefficient in the energy range dominated by DR resonances associated with $3s \rightarrow 3p$ core excitations. The vertical bars below the spectrum denote the $2p^6 3pn'l'$ DR resonance positions as expected on the basis of the hydrogenic Rydberg formula (Eq. 8). Note that resonances up to $n = 15$ are individually resolved. The vertical arrows around 3 eV denote the positions of the $2p^6 3d^2 {}^3F$ and $2p^6 3d^2 {}^1G$ doubly excited states. The inset shows the recombination rate coefficient at energies below 2 eV, where it is dominated by $2p^6 3p4l'$ resonances.

[15]. This value is the weighted average of the $3p_{1/2}$ and $3p_{3/2}$ limits. The $3p$ fine structure splitting of 0.057169 eV is not resolved. Additionally, the $2p^6 3d3l$ and $2p^6 3d4s$ resonances associated with the $3s \rightarrow 3d$ excitation are expected to appear at these low energies. As pointed out by Orban et al. [12], in this range the most notable $3s \rightarrow 3d$ contributions are due to $2p^6 3d^2 {}^3F$ and $2p^6 3d^2 {}^1G$ doubly excited states whose energy positions are determined in our experimental data to 2.97 and 3.13 eV, respectively.

The experimental energy scale was fine-tuned by multiplying the nominal electron-ion collision energies with an energy independent factor, so that so that the positions of the $2p^6 3pn'l'$ ($7 \leq n \leq 10$) resonances matched their calculated positions. For the high- n values the position of the Rydberg resonances can be estimated from the hydrogenic Rydberg formula

$$E_n = E_\infty - R \frac{q^2}{n^2}, \quad (8)$$

with the Rydberg constant R and the charge state $q = 3$ of the initial Si IV ion. The calibration factor for the energy axis deviated from unity by less than 1%.

The much less intense $2p^6 3dn'l'$ resonances with $n' \geq 4$ associated with $3s \rightarrow 3d$ core excitations are expected to occur in the energy range 9–20 eV. The recombination rate coefficient measured in this energy range, using the thermionic cathode, is shown in Figure 2. Individual resonances of the associated Rydberg series are barely visible with rather large statistical uncertainties. Nev-

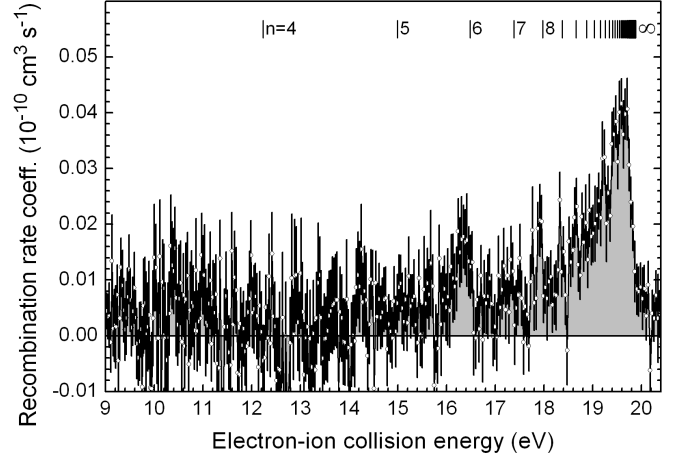


FIG. 2: Measured Si IV to Si III merged-beams electron-ion recombination rate coefficient in the energy range of DR resonances associated with $3s \rightarrow 3d$ core excitations. The vertical bars denote the $2p^6 3dn'l'$ DR resonance positions as expected on the basis of the hydrogenic Rydberg formula [Eq. (8)]. The error bars on each data point show the statistical uncertainties.

ertheless the $2p^6 3dn'l'$ series limit at 19.884 eV [15] is clearly discernable. The maximum of the DR rate coefficient at the $2p^6 3dn'l'$ series limit is about two orders of magnitude smaller than that at the $2p^6 3pn'l'$ series limit. The energy range 20–69 eV is not shown because there is no significant structure exceeding $10^{-12} \text{ cm}^3 \text{ s}^{-1}$, but in principle it comprises $2p^6 nl n'l'$ resonances associated with $3s \rightarrow nl$ excitation with $n \geq 4$.

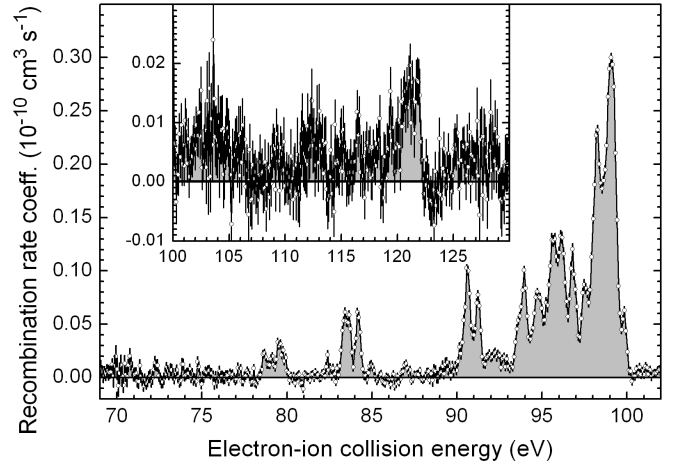


FIG. 3: Measured Si IV to Si III merged-beams recombination rate coefficient in the electron-ion collision-energy region of resonances associated with $\Delta N \geq 1$ $2s \rightarrow nl$ and $2p \rightarrow nl$ ($n \geq 3$) inner shell core excitations.

In Figure 3 we show the measured merged-beams recombination rate coefficient in the energy range 69–130 eV. This was measured using the thermionic cathode. The resonances in this energy range are associated

with $\Delta N \geq 1$ DR via $2p \rightarrow nl$ ($n \geq 3$) inner shell core excitations. Due to the large number of excitations in the displayed energy range (cf. Table I) it is prohibitive to assign individual resonances. The main contribution to the rate coefficient is most probably due to $2p \rightarrow 3l$ core excitations. Theoretical calculations suggest that DR by $2s$ excitations is insignificant [37]. The energy range from 130 up to 186 eV was also scanned and found to fluctuate with peak-to-peak variations up to $\pm 10^{-12} \text{ cm}^3 \text{ s}^{-1}$, not showing any significant structure.

The calculated RR rate coefficient as well as 25 DR resonances fitted to the measured DR spectrum in the energy region below 1.5 eV is shown in Figure 4. This fit is independent of the theoretical predictions and is explained in detail in Section V A. For the comparison with the theoretical calculation shown in the Figures 5, 6, and 7 the non-resonant RR contribution was subtracted from the measured merged-beams recombination rate coefficient at all energies. The merged-beams RR rate coefficient was derived by convolving the RR cross section with the experimental electron energy distribution. The RR cross section was calculated with a hydrogenic formula [Eq. (12) of Ref. 6], taking into account field ionization of loosely bound high Rydberg electrons inside the storage ring bending magnets Schippers et al. [6].

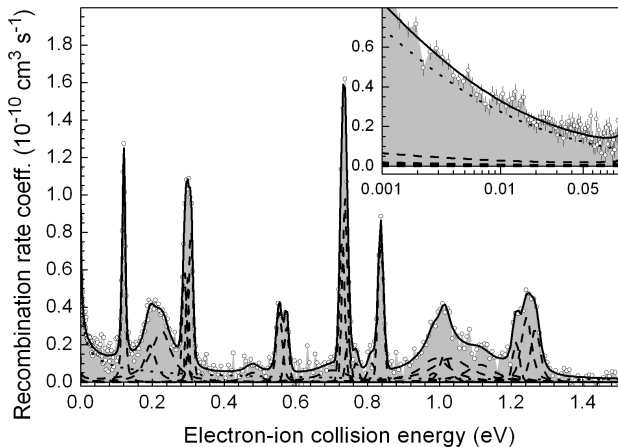


FIG. 4: Measured Si IV to Si III merged-beams rate coefficient at energies below 1.5 eV (circles and grey shaded area). The solid curve is the sum of a fit comprising 25 fitted DR resonances (dashed curves cf. Sec. V A) and the non-resonant rate coefficient due to RR (dotted curve). The inset shows the same curves, but in more detail in the energy range 1–100 meV.

B. Theoretical results

To simulate the observed DR spectra at different energies of the initially free electron, detailed computations have been carried out for the $3s \rightarrow 3p n'l'$ ($n' = 3, \dots, 6$) and $3s \rightarrow 3d n'l'$ ($n' = 3, \dots, 6$) resonant electron cap-

ture and its subsequent radiative stabilization. The first DR resonance ($3p 4d^1 D_2$) is found at about 0.1 eV, i.e., very close to zero energy of the incident electron. The exact energies and strengths of resonances close to the threshold are particularly important for the determination of reliable plasma recombination rate coefficients at low electron temperatures. Therefore, special care was taken with regard to the doubly-excited magnesium-like states from the $3l n'l'$ ($n' \geq 3$) final configurations of the recombined ion.

For the 0–6 eV low-energy part of the DR spectrum, a series of computations has been carried out. In the first approach, we included all the levels within the $3l 3l'$ and $3l 4l'$ configurations of the recombined ion. Apart from these low-lying levels with energies both below and above the threshold, we incorporated in a further step also the levels of the $3l 5l'$ and $3l 6l'$ configurations as well as later all the $nl n'l'$ levels with $n \leq 5$ and $n' \leq 6$, respectively. To keep the number of CSF manageable, levels with higher n and n' were not treated. As known from previous computations [38, 39] for the low-lying levels of multiply charged ions, such a systematic enlargement of the wave function expansion (4) typically improves the positions of the resonances significantly. For magnesium-like ions, moreover, many of the $3l n'l'$ configurations ‘overlap’ with each other in energy and, hence, ‘new’ resonances may appear in the calculated low-energy part of the theoretical DR spectrum, if the configuration space is increased. Using the single and double excitations from above, we obtained an expansion of up to 1073 CSF for the intermediate and the final-state wave functions of the Si III ions.

For the $2p \rightarrow 3l n'l'$ part of the DR spectrum we could include only levels of $2p^5 3s 3l 3l'$ and $2p^5 3s 3l 4l'$, since the number of open shells involved is increased as compared to the $3s \rightarrow 3l n'l'$ excitations. In the calculation the associated resonances appeared in the energy region 69–94 eV of the incident electrons. For these inner-shell excited spectra, further contributions from the core polarization or core-core excitations need to be omitted owing to the size requirements of the corresponding wave function expansions. The incorporation of double excitations from the $2s$ and $2p$ shells would result in expansions of several hundred thousand CSF, i.e., a size which is unfeasible for the computation of DR and autoionization properties.

Figure 5 displays the experimental Si IV DR spectrum in the energy region of 0–1.5 eV, with the nonresonant ‘background’ subtracted from the experimental results. In this figure, the observed spectrum is compared with theoretical results from different approximations. In all of these calculations, our ‘best’ wave function expansion has been applied, including the single and double excitations as discussed above. The computations differ however in the set of the one-electron orbital functions used for the representation of the initial sodium-like ions. Figure 5(a), for instance, shows the spectrum in which both the initial and final states of the recombined ion

were described by a *common* set of orbitals, neglecting the rearrangement of the electron density in the course of the dielectronic capture (or decay) of the ions. Apparently, quite a strong effect arises from this rearrangement of the electron density as seen from Figure 5(b) and 5(c), for which two independent sets of orbital functions were utilized in the representation of the initial and the recombined ion states. Figures 5(b) and 5(c) only differ in the treatment of the exchange interaction for the incoming electron. While Figure 5(b) shows the simulation for a static potential due to the charge distribution of the initial ion ('no exchange'), 5(c) incorporates the exchange interaction of the incident electron with regard to the bound-state density. Therefore, Figure 5(c) represents our best approximation within the MCDF approach. Despite the fact that the orbitals are not quite orthogonal in the computation of the two-particle matrix elements, the Auger amplitudes [Eq. (6)] were evaluated by using the techniques of Racah's algebra, i.e., for assuming orthogonality for all *inactive* electrons in these transition amplitudes [40].

Figure 5(d) displays the comparison of the present experimental data with the RMBPT result of Orban et al. [12] convolved with the electron energy distribution of the TSR photocathode electron beam. Compared to their experiment, where electron beam temperatures $k_B T_{\parallel} = 0.25$ meV and $k_B T_{\perp} = 10$ meV were found, the energy resolution is higher in the present experiment. ($k_B T_{\parallel} = 0.035$ meV, $k_B T_{\perp} = 0.9$ meV, see Section III). Our high-resolution experiment provides a more stringent test of the RMBPT calculation which represents the measurement almost perfectly but cannot easily be extended to energies beyond 1.4 eV where an increasing number of resonances can contribute to the DR spectrum.

Table II displays the assignment and position of the 28 lowest resonances in the energy region $E_{\text{res}} \lesssim 1.5$ eV calculated with the MCDF method as well as the corresponding RMBPT results of Orban et al. [12]. In addition to the energies of these resonances, this table also includes the weights of the dominant *LS* terms as well as the resonance strengths. The weights of the leading *LS* terms have been obtained by a unitary transformation of the wave functions from the *jj*-coupled into a *LS*-coupled basis [41]. While the lowest 11 resonances appear rather pure in *LS* coupling ($\gtrsim 92\%$), some larger admixtures are found for a few of the higher-lying resonances. As mentioned above, all data in this table correspond to our best representation of the resonances and by including the effects of the rearrangement of the electron density and the exchange interaction (cf. Fig. 5c). The lowest resonances in the $3s \rightarrow 3p n'l'$ part of the DR spectrum belong to the $3p4d^1 D_2^o$ level, followed by the fine-structure levels of the $3p4d^3 F^o$ term. Apparently, all levels from the $3p^2$ and $3p3d$ configurations are below the DR threshold.

At energies below 0.9 eV the RMBPT results of Orban et al. [12] are in excellent agreement with the present measurements [Fig. 5(d)]. At higher energies, where

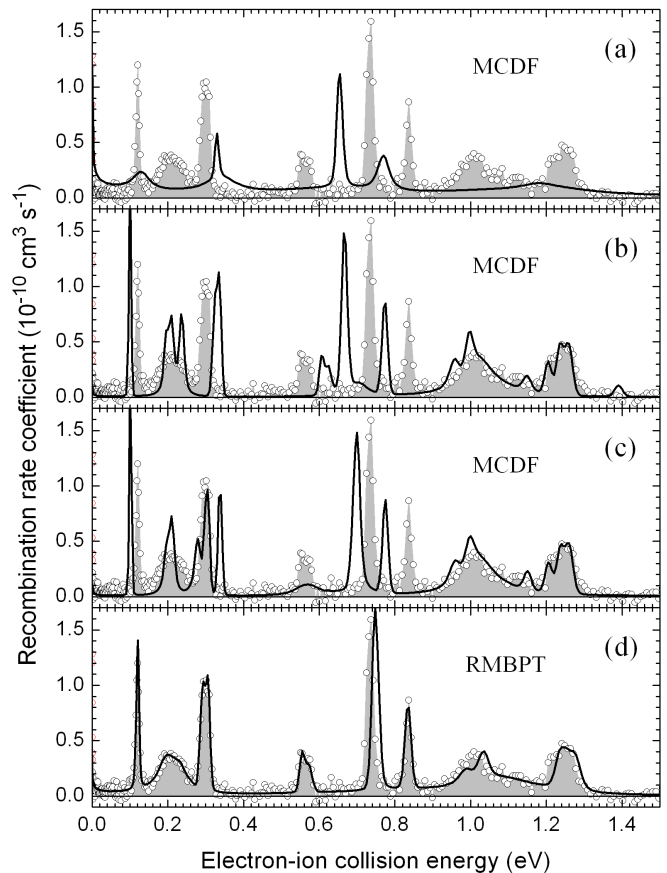


FIG. 5: Comparison of the experimental Si IV DR spectrum (open circles) in the energy region 0–1.5 eV with various theoretical results (solid curves). Figures (a), (b), and (c) show our multiconfiguration Dirac-Fock (MCDF) method results and (d) published relativistic many-body perturbation theory (RMBPT) calculations (Ref. [12]). The nonresonant part of the recombination rate coefficient due to radiative recombination (RR) was subtracted from the measured curve (see text). In the MCDF calculation three different approximations have been applied to the enlarged CSF basis including all the fine-structure states from the $nl n'l'$ ($n, n' = 3, 4, 5, 6$) configurations: (a) using the orbital functions from the doubly-excited $3l n'l' 2S+1 L_J$ levels for the representation of both, the initial and final states; (b) with an independent optimization of the sodium- and magnesium-like states but without including the exchange interaction between the initially free electron and the bound-state electrons; (c) the same as in (b) but by incorporating the exchange interaction with regard to the bound-state density.

the MCDF results reproduce the experimental findings slightly better than at lower energies, the RMBPT resonance positions are at somewhat too high energies as can also be seen in the comparison with the experimental data of Orban et al. [12]. In our work, this slight discrepancy is more pronounced because of the increased experimental resolution and because of reduced statistical uncertainties in the present experiment. With a few exceptions, MCDF and RMBPT resonance energies

TABLE II: Comparison of the present multiconfiguration Dirac-Fock (MCDF) resonance parameters with the results of the relativistic many-body perturbation theory (RMBPT, Ref. [12]) for all $3p\ 4l$ and $3p\ 5s$ DR resonances associated with $3s \rightarrow 3p$ core excitations. The listed quantities are resonance energies E_{res} and strengths S [Eq. (1)]. The dominant LS-terms of the resonance states are given in the first column along with their weights in the representation of the wave functions. The weights are derived from the MCDF calculation. The states are listed in the order of increasing MCDF resonance energies. RMBPT resonance energies which appear in a different order [12] are marked by an asterisk in the third column.

dominating LS term	E_{res} (eV)		S (10^{-20} eV cm ²)	
	MCDF	RMBPT	MCDF	RMBPT
$3p\ 4d\ ^1D_2$ (96%)	0.102	0.121	8.33	6.88
$3p\ 4d\ ^3F_2$ (94%)	0.198	0.191	3.49	3.77
$3p\ 4d\ ^3F_3$ (97%)	0.212	0.204	4.55	4.95
$3p\ 4d\ ^3F_4$ (99%)	0.280	0.233	4.46	5.58
$3p\ 4d\ ^3D_1$ (95%)	0.299	0.288	1.83	1.78
$3p\ 4d\ ^3D_2$ (94%)	0.307	0.296	2.96	2.96
$3p\ 4d\ ^3D_3$ (94%)	0.339	0.307	3.76	4.01
$3p\ 4d\ ^3P_2$ (95%)	0.557	0.556	1.57	1.42
$3p\ 4d\ ^3P_1$ (95%)	0.583	0.572	0.91	0.83
$3p\ 4d\ ^3P_0$ (95%)	0.633	0.581	0.28	0.27
$3p\ 4f\ ^3F_2$ (93%)	0.691	0.744	1.38	1.72
$3p\ 4f\ ^3F_4$ (77%)	0.702	0.754	3.10	3.20
$3p\ 4f\ ^3F_3$ (92%)	0.702	*0.748	2.65	2.50
$3p\ 4f\ ^1G_4$ (68%)	0.709	0.796	1.70	1.46
$3p\ 4f\ ^1F_3$ (99%)	0.775	0.835	3.14	2.96
$3p\ 5s\ ^3P_0$ (73%)	0.945	0.976	0.25	0.24
$3p\ 5s\ ^3P_1$ (72%)	0.960	0.991	0.74	0.71
$3p\ 4f\ ^3G_3$ (98%)	0.995	1.048	2.33	2.48
$3p\ 5s\ ^3P_2$ (74%)	0.999	*1.031	1.20	1.14
$3p\ 4f\ ^3G_4$ (98%)	1.013	1.067	2.94	3.13
$3p\ 4f\ ^3G_5$ (98%)	1.034	1.088	3.54	3.75
$3p\ 4d\ ^1F_3$ (79%)	1.087	*0.654	1.58	2.23
$3p\ 5s\ ^1P_1$ (73%)	1.151	1.133	0.84	0.78
$3p\ 4f\ ^3D_2$ (85%)	1.207	1.276	1.10	1.01
$3p\ 4f\ ^3D_3$ (97%)	1.238	*1.254	1.66	1.56
$3p\ 4f\ ^1D_2$ (90%)	1.258	*1.235	1.16	1.13
$3p\ 4f\ ^3D_1$ (97%)	1.266	1.282	0.70	0.65
$3p\ 4d\ ^1P_1$ (73%)	1.393	*1.040	0.46	0.54

agree with one another to within ~ 50 meV, often even to within ~ 20 meV.

Figures 6 and 7 display our theoretical MCDF DR spectrum compared with experiment for $\Delta N = 0$ and $\Delta N = 1$ DR. As described above, all $nl\ n'l'$ configurations with $3 \leq n, n' \leq 6$ have been taken into account for $\Delta N = 0$ DR. The incorporation of further configurations with even higher principal quantum numbers n' has no effect upon the low-lying resonances for energies $E_{\text{res}} \lesssim 6$ eV above the threshold. Although the basic features are well described in these spectra, some deviations in the positions and strengths of the peaks remain which we attribute to neglected correlation and many-electron effects in the system.

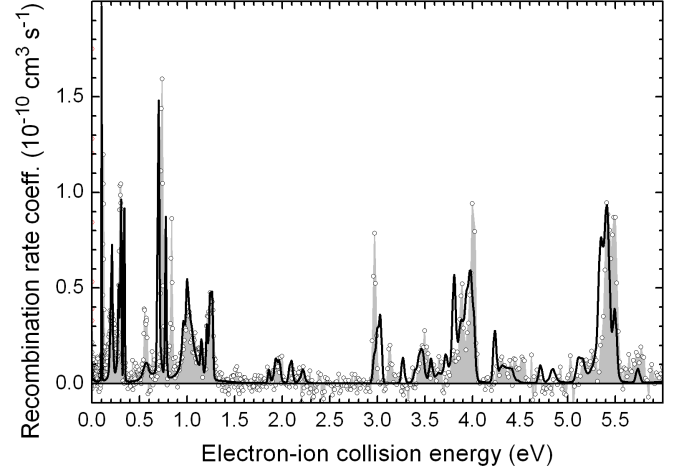


FIG. 6: Comparison of the experimental Si IV DR spectrum (open circles) in the energy region 0 – 6 eV with the final result of the MCDF calculation (solid line). This energy range includes $2p^6\ 3p\ n'l'$ ($4 \leq n' \leq 6$) and $2p^6\ 3d^2$ resonances. The nonresonant part of the recombination rate coefficient due to RR was subtracted from the measured curve (see text)

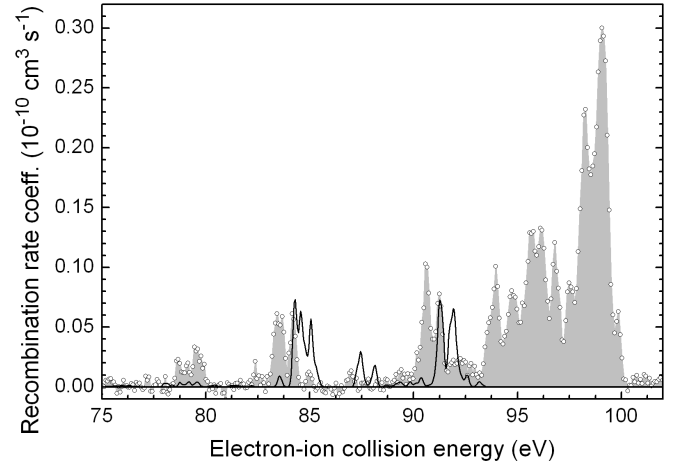


FIG. 7: Comparison of experimental Si IV DR spectrum (open circles) in the energy region of the $2p^5\ 3s\ 3l\ n'l'$ resonances with the results of our MCDF calculation (solid line). The nonresonant part of the recombination rate coefficient due to RR was subtracted from the measured curve (see text)

In addition to calculations of the low-lying resonances associated with $3s \rightarrow 3p$ and $3s \rightarrow 3d$ core excitations, computations have been carried out also for all $2p^5\ 3s\ 3l\ 3l'$ and $2p^5\ 3s\ 3l\ 4l'$ resonances which are found to occur starting at 69 eV. For this high-energy part of the spectrum, we expect only a rough agreement between our computations and experiment as the electronic structure of the intermediate resonances now includes *four* open shells which do not allow any systematic enlargement of the configuration basis. For this part of the spectrum, therefore, the computations have been restricted to allow only one electron in the $n = 4$ shell. As seen in

Figure 7, only some of the resonances at 84 and 91 eV are reproduced by our simulations but they are shifted upwards in energy by about 1 eV.

Apart from the radiative stabilization of the intermediate resonances by E1 electric-dipole decay, we explored also the effects of higher multipoles (M1, E2, M2) in the coupling of the radiation field. These ‘multipoles’ are well suppressed for neutral systems by at least 5 orders of magnitude but become important for highly-charged ions. For the initially triply ionized Si IV ions, these contributions are still negligible at the present level of accuracy for the simulation of the DR spectra in Figures 5–7.

V. PLASMA RATE-COEFFICIENTS

DR rate coefficients for a Maxwellian plasma can be derived from the experimental merged-beams recombination rate coefficient and the theoretical cross section. This is done in the following sections. Of particular interest for astrophysical model calculations are the plasma DR rate coefficients in the electron temperature ranges where Si IV is formed in astrophysical plasmas. The approximate temperature range where Si IV forms in photoionized and collisionally ionized plasmas can be obtained from the work of Kallman and Bautista [42] and Bryans et al. [43], respectively. For photoionized plasmas, Kallman and Bautista [42] find that the fractional Si IV abundance peaks at a temperature of 1 eV. The ‘photoionized zone’ may be defined as the temperature range where the fractional abundance of a given ion exceeds 10% of its peak value. For Si IV this corresponds to a temperature range of 0.8–1.4 eV. Using the same criterion and the fractional abundances of Bryans et al. [43], for coronal equilibrium the Si IV ‘collisionally ionized zone’ is estimated to extend over a temperature range of 4–10 eV. It should be kept in mind that these temperature ranges are only indicative. They depend, in part, on the accuracy of the underlying atomic data base.

A. Derivation of the plasma DR rate coefficients

The DR rate coefficient in a Maxwellian plasma is derived by convolving the DR cross section σ_{DR} with an isotropic Maxwell-Boltzmann electron energy distribution as detailed by Schippers et al. [6, 44]. To derive a meaningful plasma DR rate coefficient from a total merged-beams rate coefficient there are some issues that require special consideration.

Interference between DR and RR is typically unimportant [45]. Hence here we subtract, the non-resonant RR contribution from the measured merged-beams recombination rate coefficient. The applied merged-beams RR rate coefficient was the same as used for the correction of the recombination rate coefficient [Eq. (7)] at the reference point as well as that which was subtracted from the experimental merged-beams recombination rate

coefficient for comparison with theoretical results (cf. Sec. IV A).

When the electron-ion collision energy E is larger than the experimental energy spread ΔE , one can use $\alpha_{\text{DR}}/(2E/m_e)^{1/2}$ instead of σ_{DR} for the convolution. When $E \lesssim \Delta E$, the energy spread influences the outcome of the convolution of the cross section. In order to account for this effect, the low energy DR cross section was extracted by fitting 25 DR resonance line-shapes to the measured DR spectrum in the energy region below 1.5 eV (Fig. 4), independent of the theoretical predictions above (see Ref. [44] for a more detailed description of the method).

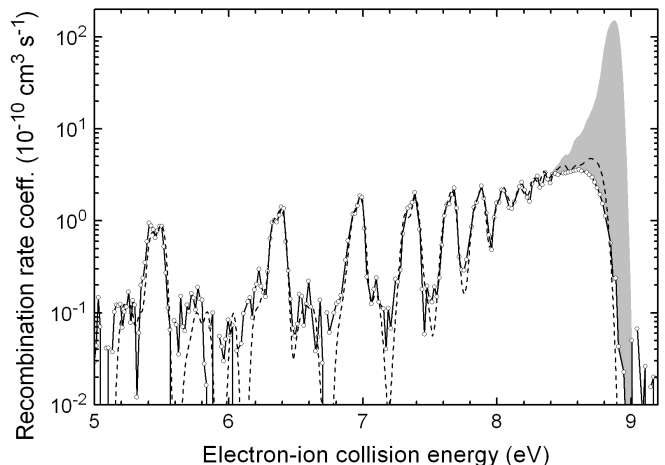


FIG. 8: Comparison between the experimental merged-beams DR rate coefficient (open circles with solid line) and the AUTOSTRUCTURE calculation. The AUTOSTRUCTURE calculation was multiplied by a factor of 1.13 (see text). The dashed line is the theoretical result with account for the experimental field ionization of high- n Rydberg states using the field ionization model of [6]. The shaded area highlights the unmeasured purely calculated part of the composite DR rate coefficient.

Field ionization of the loosely bound high Rydberg electron in the recombined ions can result from the motional electric fields that the ions experience inside the storage ring bending magnets [6]. The ion beam on its way to the detector passes the strongest electrical field in the dipole bending magnet in front of the detector. From this electric field the critical quantum number for field ionization is $n_{\text{crit}} = 17$, i.e., in the present experiment only RR and DR involving capture into Rydberg levels with quantum numbers less than 17 contribute fully to the measured merged-beams recombination rate coefficient. Due to radiative decay of higher Rydberg states on the way from the interaction section to the detector, the field ionization cutoff is not sharp but somehow smeared out to $n \geq 17$. Similar to the approach of Schippers et al. [6, 44] the missing DR resonance strength up to $n_{\text{max}} = 1000$ was estimated from a theoretical calculation using the AUTOSTRUCTURE code [28]. $n_{\text{max}} = 1000$ is an arbitrary upper limit beyond which no significant

contribution to the total DR cross section is expected. Although the AUTOSTRUCTURE code does not reproduce the resonance structure below 5 eV (cf. Fig. 1 of [9]) as accurately as our present MCDF calculations, it reproduces the more regular structures of Rydberg resonances between 5 eV and 8.4 eV when the calculated rate coefficient is multiplied by a constant factor of 1.13. The unmeasured DR contribution due to $n \geq 17$ exceeds the measured contribution by more than one order of magnitude. This is shown in Figure 8. The DR contribution for $\Delta N = 0$ $3s \rightarrow 3p$ DR from $n = 17$ –1000 was added to the measured spectrum by adding the difference between the measured rate coefficient and the adjusted AUTOSTRUCTURE result in the energy range 8.39 eV – 9.01 eV (grey shaded area in Figure 8).

The $3s \rightarrow 3d$ $\Delta N = 0$ series with its limit at about 20 eV was not corrected for field ionization losses of high Rydberg states because its contribution is negligible compared to the $3s \rightarrow 3p$ $\Delta N = 0$ series limit. As the strengths of resonances contributed by $\Delta N \geq 1$ DR fall much faster with increasing n than the strength of $\Delta N = 0$ DR resonances, and because of the much smaller contribution of $\Delta N \geq 1$ DR, the field ionized contribution for $\Delta N \geq 1$ DR with $n \geq 17$ was also not corrected for field ionization losses, either.

The non-measured contribution to the plasma DR rate coefficient ranges in the photoionized zone from only 1% at 0.8 eV to 36% at 1.4 eV. It has its maximum (83%) at a plasma electron temperature of $k_B T_e = 7.9$ eV. In the collisionally ionized zone the contribution ranges from 79% at 4 eV to 83% at 10 eV. The contribution falls off slightly towards higher temperatures and is still 72% at 1000 eV. The resulting plasma DR rate coefficient with and without the correction of field ionization losses is shown in Figure 9.

For convenient use in astrophysical modeling codes the Si IV to Si III plasma DR rate coefficient $\alpha_p^{(\text{DR})}$ was fitted using

$$\alpha_p^{(\text{DR})}(T_e) = (T_e)^{-3/2} \sum_{i=1}^9 c_i \exp(-E_i/k_B T_e). \quad (9)$$

The fitting parameters c_i and E_i are given in Table III. The fit deviates by less than 1% from the experimentally-derived result in the temperature range 0.01 eV – 10000 eV.

B. Comparison with present theory

In Figure 9 we compare the plasma DR rate coefficient derived from the MCDF calculation in the electron-ion collision energy range 0–6 eV and a plasma DR rate coefficient derived from DR merged-beams resonances measured in the same electron-ion collision energy range. We find good agreement in the comparison of these two plasma DR rate coefficients. The plasma DR rate coefficient generated by DR resonances, calculated by means

TABLE III: Parameters for the fit of Equation (9) to the experimental plasma DR rate coefficient. Numbers in square brackets denote powers of 10.

i	c_i ($\text{cm}^3 \text{s}^{-1} \text{K}^{3/2}$)	E_i (eV)
1	2.13[−8]	1.02[−2]
2	6.12[−8]	5.00[−2]
3	1.10[−6]	1.24[−1]
4	3.65[−6]	2.44[−1]
5	1.45[−5]	6.90[−1]
6	1.78[−5]	1.53[+0]
7	3.05[−4]	5.43[+0]
8	9.50[−3]	8.81[+0]
9	1.89[−3]	8.05[+1]

of the MCDF method for electron-ion collision energies below 6 eV is somewhat lower than the rate coefficient generated from the experimentally-derived resonances in the same energy range. Between $k_B T_e = 0.01$ eV and $k_B T_e = 0.04$ eV the agreement is better than 12%. Above a plasma electron temperature of $k_B T_e = 0.04$ eV the agreement is even better than 7%.

C. Comparison with previous results

In Figure 9 we also compare our experimentally-derived DR rate coefficient with the experimental result of Orban et al. [9] and with recent theoretical results of Gu [46] and Altun et al. [37].

In the collisionally ionized zone the rate coefficient of Gu [46] overestimates our experimentally-derived plasma DR rate coefficient by about 10%. In contrast, the plasma DR rate coefficient of Altun et al. [37] underestimates the experimentally-derived plasma DR rate coefficient in the collisionally ionized zone by about 10%. These deviations are within the experimental uncertainty. The difference between the two codes of about 20% also gives an idea as to the uncertainty of these state-of-the-art DR calculations.

In the photoionized zone the experimentally-derived plasma DR rate coefficient is decisively determined (between 93% at 0.8 eV and 41% at 1.4 eV) by the $3s + e^- \rightarrow 3p4l'$ resonances which occur at electron-ion collision energies below 1.5 eV. The calculations of Gu [46] and Altun et al. [37] comprise DR for all $\Delta N = 0$ channels including the $3p4l'$ resonances. Despite the convolution of the DR cross section with the plasma electron energy distribution one can recognize that the calculations of Gu [46] and Altun et al. [37] either underestimate the strengths of the $3p4l'$ resonances at low energies or overestimate their energy positions. We can reproduce the qualitative trend of their plasma DR rate coefficients by shifting our experimentally derived $3p4l'$ resonances to higher energies by about 0.15 eV. Both theoretical plasma DR rate coefficients underestimate the experimentally-derived rate coefficient in the photoion-

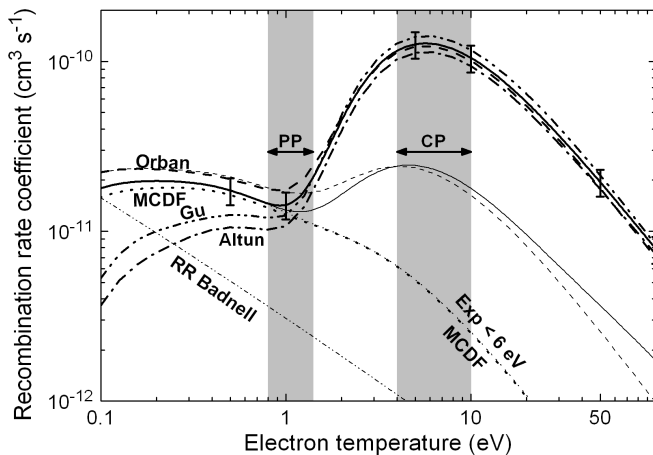


FIG. 9: Experimentally derived Si IV to Si III DR rate coefficient in a plasma (thick solid line) comprising $\Delta N = 0$ DR (Figs. 1 and 2), $\Delta N = 1$ and 2 DR (Fig. 3), and the theoretical estimate for the unmeasured contributions of states with $n \geq 17$ for $\Delta N = 0$ DR (Fig. 8). The error bars denote the $\pm 18\%$ (1σ) experimental uncertainty in the absolute rate coefficient. The experimental results without DR extrapolation is shown by the thin solid line. Also shown are recent theoretical calculations of the DR rate coefficient by Gu [46] (thick dash-dot-dotted line, labeled Gu) and Altun et al. [37] (thick dash-dotted line, labeled Altun), and the recent experimental DR rate coefficient by Orban et al. [9] (thick dashed line, labeled Orban). The contribution from the experimentally measured DR resonances between 0 and 6 eV is shown as the thin dotted line (labeled Exp < 6 eV) while the contribution of the MCDF calculation in the same energy range is shown as thick dotted line (labeled MCDF). A recent calculation of the plasma RR by Badnell [47] is shown as the thin dash-dot-dotted line labeled RR Badnell. The temperature ranges where Si IV is expected to peak in abundance in photoionized plasmas (labeled PP) and collisionally ionized plasmas (labeled CP) are highlighted.

ized zone. The rate coefficient of Altun et al. [37] is a factor of 0.71–0.86 lower than the experimentally derived rate coefficient. For the rate coefficient of Gu [46] the factor is 0.83–1.02.

The comparison of our experimentally derived plasma DR rate coefficient with the experimental result of Orban et al. [9] shows, that both data sets agree to within 25% in the temperature range 0.1–1000 eV. In the photoionized zone the plasma DR rate coefficient of Orban et al. [9] is 18%–24% larger than our result. This larger deviation than in the collisionally ionized zone is probably associated with differences in the data reduction process. In the collisionally ionized zone the plasma DR rate coefficient of Orban et al. [9] is less than 5% lower than our result. The increasing deviation between the two

plasma DR rate coefficients above ≈ 30 eV is probably attributed to the fact that, in contrast to the work of Orban et al. [9], the present experimentally derived DR rate coefficient also includes $\Delta N = 1$ and even $\Delta N > 1$ DR.

VI. CONCLUSIONS

Electron-ion recombination of Si IV forming Si III was studied both experimentally using the merged-beams method at a heavy ion storage ring and theoretically by employing the MCDF method. We see good agreement in DR resonance strength and positions between the experiment and the MCDF calculations for $\Delta N = 0$ DR in the investigated electron-ion collision energy range 0–6 eV. Below an energy of 1.4 eV the accuracy in the energy positions was better than 70 meV, the position of the resonance at the lowest energy was even accurate to within 20 meV. A great advantage of the MCDF method is that it is conceptually much simpler to implement than other many-body techniques and, hence, can be applied also to more complex shell structures — if enough computational resources are available. We currently plan to extend the code in order to make computations feasible for atoms and ions with (initially) two or three electrons in their valence shell.

The present experimentally derived Si IV plasma DR rate coefficient agrees with the experimental result of Orban et al. [9], to within the combined experimental errors. We found good agreement between the theoretical results of Gu [46] and Altun et al. [37] and our experimental result in the temperature range where Si IV forms in collisionally ionized plasmas. The agreement is reasonable at temperatures where Si IV is predicted to form in photoionized as. At temperatures below this the agreement becomes significantly worse with decreasing temperature. These findings demonstrate the necessity of benchmarking theoretical results with experiment, because modern theory still has difficulty calculating resonance energies reliably when the electron-ion collision energy and Rydberg level of the recombined ion are small.

Acknowledgments

We gratefully acknowledge the excellent support by the MPI-K accelerator and TSR crews. This work was supported in part by the German federal research-funding agency DFG under contract no. Schi 378/5 and Fr 1251/13. DL and DWS were supported in part by the NASA Astronomy and Astrophysics Research and Analysis program and the NASA Solar and Heliospheric Physics program.

[1] D. Lukić, D. W. Savin, M. Schnell, C. Brandau, E. W. Schmidt, S. Böhm, A. Müller, S. Schippers, M. Lestinsky,

F. Sprenger, et al., *Astrophys. J.* **664**, 1244 (2007).
[2] D. W. Savin, *Astrophys. J.* **533**, 106 (2000).

- [3] S. A. Levshakov, I. I. Agafonova, M. Centuri3n, and I. E. Mazets, *Astron. Astrophys.* **383**, 813 (2002).
- [4] A. Aguirre, J. Schaye, T.-S. Kim, T. Theuns, M. Rauch, and W. L. W. Sargent, *Astrophys. J.* **602**, 38 (2004).
- [5] G. J. Ferland, K. T. Korista, D. A. Verner, J. W. Ferguson, J. B. Kingdon, and E. M. Verner, *Publ. Astron. Soc. Pac.* **110**, 761 (1998).
- [6] S. Schippers, A. M3ller, G. Gwinner, J. Linkemann, A. A. Saghir, and A. Wolf, *Astrophys. J.* **555**, 1027 (2001).
- [7] S. B3hm, A. M3ller, S. Schippers, W. Shi, M. Fogle, P. Glans, R. Schuch, and H. Danared, *Astron. Astrophys.* **437**, 1151 (2005).
- [8] S. B3hm, A. M3ller, S. Schippers, W. Shi, N. Ekl3w, R. Schuch, H. Danared, and N. R. Badnell, *Astron. Astrophys.* **405**, 1157 (2003).
- [9] I. Orban, P. Glans, Z. Altun, E. Lindroth, A. K3llberg, and R. Schuch, *Astron. Astrophys.* **459**, 291 (2006).
- [10] J. Linkemann, A. M3ller, J. Kenntner, D. Habs, D. Schwalm, A. Wolf, N. R. Badnell, and M. S. Pindzola, *Phys. Rev. Lett.* **74**, 4173 (1995).
- [11] M. Fogle, N. R. Badnell, N. Ekl3w, T. Mohamed, and R. Schuch, *Astron. Astrophys.* **409**, 781 (2003).
- [12] I. Orban, E. Lindroth, P. Glans, and R. Schuch, *J. Phys. B* **40**, 1063 (2007).
- [13] D. Schneider, R. Bruch, A. Shlyaptseva, T. Brage, and D. Ridder, *Phys. Rev. A* **51**, 4652 (1995).
- [14] Y. Ralchenko, F.-C. Jou, D. E. Kelleher, A. E. Kramida, A. Musgrove, J. Reader, W. L. Wiese, and K. Olsen, *NIST Atomic Spectra Database :version 3.1.0:* (National Institute of Standards and Technology, Gaithersburg, MD, 2006), available: <http://physics.nist.gov/asd3>.
- [15] Y. G. Toresson, *Ark. Fys.* **18**, 179 (1960).
- [16] M. Tokman, N. Ekl3w, P. Glans, E. Lindroth, R. Schuch, G. Gwinner, D. Schwalm, A. Wolf, A. Hoffknecht, A. M3ller, et al., *Phys. Rev. A* **66**, 012703 (2002).
- [17] I. P. Grant, in *Methods in Computational Chemistry*, edited by S. Wilson (Plenum Press, New York, 1988), vol. 2, p. 1.
- [18] S. Fritzsche, *Phys. Scr.* **T100**, 37 (2002).
- [19] F. A. Parpia, C. F. Fischer, and I. P. Grant, *Comput. Phys. Commun.* **94**, 249 (1996).
- [20] S. Fritzsche, *J. Elec. Spectrosc. Rel. Phenom.* **114-116**, 1155 (2001).
- [21] S. Fritzsche, A. Surzhykov, and T. St3hlker, *Phys. Rev. A* **72**, 012704 (2005).
- [22] S. Fritzsche, C. F. Fischer, and C. Z. Dong, *Comput. Phys. Commun.* **124**, 340 (2000).
- [23] P. Zimmerer, N. Gr3n, and W. Scheid, *Phys. Lett. A* **148**, 457 (1990).
- [24] M. H. Chen, *Phys. Rev. A* **41**, 4102 (1990).
- [25] N. R. Badnell and M. S. Pindzola, *Phys. Rev. A* **43**, 570 (1991).
- [26] S. Fritzsche, G. Zschornack, G. Musiol, and G. Soff, *Phys. Rev. A* **44**, 388 (1991).
- [27] S. Fritzsche, B. Fricke, and W.-D. Sepp, *Phys. Rev. A* **45**, 1465 (1992).
- [28] N. R. Badnell, *J. Phys. B* **19**, 3827 (1986), <http://amdpp.phys.strath.ac.uk/autos/>.
- [29] G. Kilgus, D. Habs, D. Schwalm, A. Wolf, N. R. Badnell, and A. M3ller, *Phys. Rev. A* **46**, 5730 (1992).
- [30] A. Lampert, A. Wolf, D. Habs, J. Kenntner, G. Kilgus, D. Schwalm, M. S. Pindzola, and N. R. Badnell, *Phys. Rev. A* **53**, 1413 (1996).
- [31] S. Pastuszka, U. Schramm, M. Grieser, C. Broude, R. Grimm, D. Habs, J. Kenntner, H.-J. Miesner, T. Sch3ßler, D. Schwalm, et al., *Nucl. Instrum. Methods A* **369**, 11 (1996).
- [32] A. M3ller and A. Wolf, in *Accelerator-based atomic physics techniques and applications*, edited by J. C. Austin and S. M. Shafroth (AIP Press, Woodbury, 1997), p. 147.
- [33] M. Grieser, M. Blum, D. Habs, R. V. Hahn, B. Hochadel, E. Jaeschke, C. M. Kleffner, M. Stampfer, M. Steck, and A. Noda, in *Proceedings of the 19th International Symposium on Cooler Rings and Their Applications, Tokyo, Japan, November 5-8, 1990*, edited by T. Katayama and A. Noda (World Scientific, Singapore, 1991), pp. 190-198.
- [34] F. Sprenger, M. Lestinsky, D. A. Orlov, D. Schwalm, and A. Wolf, *Nucl. Instrum. Methods A* **532**, 298 (2004).
- [35] H. Poth, B. Seligmann, W. Schwab, M. W3rtge, A. Wolf, R. Conti, W. Frieze, D. Gidley, A. Rich, M. Skalsey, et al., *Hyperfine Interact.* **44**, 259 (1988).
- [36] D. A. Orlov, U. Weigel, D. Schwalm, A. S. Terekhov, and A. Wolf, *Nucl. Instrum. Methods A* **532**, 418 (2004).
- [37] Z. Altun, A. Yumak, N. R. Badnell, S. D. Loch, and M. S. Pindzola, *Astron. Astrophys.* **447**, 1165 (2006).
- [38] C. Z. Dong, S. Fritzsche, B. Fricke, and W.-D. Sepp, *Mon. Not. R. Astron. Soc.* **307**, 809 (1999).
- [39] S. Fritzsche, C. Z. Dong, and E. Tr3bert, *Mon. Not. R. Astron. Soc.* **318**, 263 (2000).
- [40] S. Fritzsche, J. Nikkinen, S.-M. Huttula, H. Aksela, M. Huttula, and S. Aksela, *Phys. Rev. A* **75**, 012501 (2007).
- [41] G. Gaigalas, T. Zalandauskas, and S. Fritzsche, *Comput. Phys. Commun.* **157**, 239 (2004).
- [42] T. Kallman and M. Bautista, *Astrophys. J. Suppl. Ser.* **133**, 221 (2001).
- [43] P. Bryans, N. R. Badnell, T. W. Gorczyca, J. M. Laming, W. Mitthumsiri, and D. W. Savin, *Astrophys. J. Suppl. Ser.* **167**, 343 (2006).
- [44] S. Schippers, M. Schnell, C. Brandau, S. Kieslich, A. M3ller, and A. Wolf, *Astron. Astrophys.* **421**, 1185 (2004).
- [45] M. S. Pindzola, N. R. Badnell, and D. C. Griffin, *Phys. Rev. A* **46**, 5725 (1992).
- [46] M. F. Gu, *Astrophys. J. Suppl. Ser.* **153**, 389 (2004).
- [47] N. R. Badnell, *Astrophys. J. Suppl. Ser.* **167**, 334 (2006).